THE JOURNAL OF PHYSICAL CHEMISTRY C

Article

pubs.acs.org/JPCC

Direct Evidence of Chelated Geometry of Catechol on TiO_2 by a Combined Solid-State NMR and DFT Study

Daniel Finkelstein-Shapiro,[*,†,‡,#] Stephen K. Davidowski,[†,▽] Paul B. Lee,[¶] Chengchen Guo,[†] Gregory P. Holland,[§] Tijana Rajh,[∥] Kimberly A. Gray,[¶] Jeffery L. Yarger,[†] and Monica Calatayud[‡,⊥]

[†]Department of Chemistry and Biochemistry, Arizona State University, Tempe, Arizona 85282, United States

[‡]Laboratoire de Chimie Théorique, Sorbonne Universités, UPMC Univ Paris 06, CNRS, CC 137-4, place Jussieu F., 75252 Paris Cedex 05, France

[¶]Department of Civil and Environmental Engineering, Northwestern University, Evanston, Illinois 60202, United States

[§]Department of Chemistry and Biochemistry, San Diego State University, 5500 Campanile Drive, San Diego, California 92182-1030, United States

[∥]Center for Nanoscale Materials, Argonne National Laboratory, Argonne, Illinois 60439, United States

[⊥]Institut Universitaire de France, rue Descartes, 75231 Paris Cedex 05, France

Supporting Information

ABSTRACT: Catechol on TiO_2 is a model system for a class of molecules that bind and interact very strongly with metal oxides. This interaction gives rise to a marked charge-transfer absorption band that can be used to sensitize the complex to visible light. In solar cells, these are called type II sensitizers in contrast with type I sensitizers where an excitation of the molecule with subsequent charge injection is the main mechanism for placing an electron in the conduction band of the semiconductor. The adsorption geometry of these molecules is critical in their functioning. Nuclear magnetic resonance (NMR) spectroscopic methods can be used to elucidate structural information about the local geometry at the substrate−molecule interface. NMR methods coupled with density functional theory (DFT) allow for the detailed characterization of molecular binding modes. In the present work, we report a solid-state NMR and DFT study of catechol on TiO_2. DFT-GIPAW chemical shift predictions for the ^{13}C CP-MAS experiments unambiguously indicate the presence of a chelated geometry. $^{1}H \rightarrow {}^{13}C$ cross-polarization build-up kinetics were used to determine the protonation state of additional geometries and point toward the presence of molecular species. The most stable adsorption modes on regular slab models were found to be bidentate, and it is only in the presence of defective surfaces where the chelated mode is stabilized in the presence of undercoordinated titanium surface sites. The combined NMR and DFT approach thus allows characterization of the binding geometry, which is a stepping stone in the design of more complex light-harvesting architectures. This work constitutes, to the best of our knowledge, the first detailed instance of combined solid-state NMR and DFT studies on this class of materials.

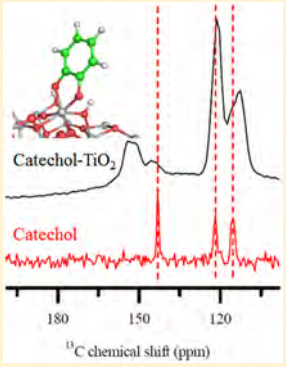

INTRODUCTION

Functionalized semiconductors are at the forefront of solar energy research due to their robustness, low cost, and versatility.[1] The high surface area and multiple anchoring sites make functionalization with different ligands straightforward. The abundance of ligand−semiconductor combinations opens pathways to improve dye-sensitized solar cells.

Sensitizers fall into two categories: type I which inject charge into the semiconductor via their excited state, and type II, which inject charge directly into the semiconductor from their ground state[2] (see Figure 1). While a number of very sophisticated chromophores and charge stabilization schemes in type I sensitizers have been made and remain a very active topic of research,[3,4] small molecule functionalization (type II sensitizers) has shown tremendous versatility, making its way into photovoltaic cells,[5] photoelectrochemical water splitting cells,[6] photoreduction,[7] electronic devices,[8] and sensors.[9] Because of the simplicity of the sensitizers used, it has also provided insight into fundamental interfacial phenomena notably the surface enhanced Raman scattering effect on semiconductors[10] and the role of vibrations in efficient charge transfer across the interface.[11] They are interesting due to their ease of synthesis and low cost. We note that the two pathways, type I and type II, also correspond to the two pathways present in Fano systems which have received renewed attention in nanostructures.[12,13]

Efficient injection and slow recombination depend critically on the molecule−semiconductor junction, characterized by the electronic coupling, which is very sensitive to the adsorption geometry.[2,14−16] Thus, a specific understanding of preferred binding configurations is a necessary step to model and improve such materials. Catechol on TiO_2 is one of the most

Received: August 9, 2016
Revised: September 21, 2016
Published: September 23, 2016

DOI: 10.1021/acs.jpcc.6b08041
J. Phys. Chem. C 2016, 120, 23625−23630

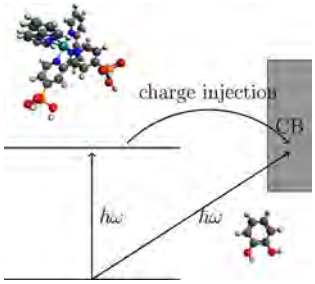

Figure 1. Energy diagram of an adsorbed molecule on a semiconductor. Two possible excitation pathways are possible: excitation to the discrete molecular state with subsequent charge injection into the semiconductor's conduction band (type I sensitization), and direct excitation into the conduction band (type II sensitization). These transition dipole moments as well as the electronic coupling dependent on the charge injection are very sensitive to the adsorption mode. Next to the pathways are two representative sensitizers: a tris(bipyridine)ruthenium(II) derivative for type I sensitization and catechol for type II sensitization.

studied model systems because it represents the simplest realization of a larger family of hybrids with very strong electronic couplings between adsorbate and semiconductor.[9] A large body of literature on the binding mode has been published since the first reference in 1991[17] and remains to date a topic of current research activity. The three proposed binding geometries in addition to molecular physisorption are (1) chelated (also called in the literature mononuclear bidentate), (2) bidentate (also called in the literature binuclear bidentate or dissociative), and (3) monodentate (Figure 2). Studies of

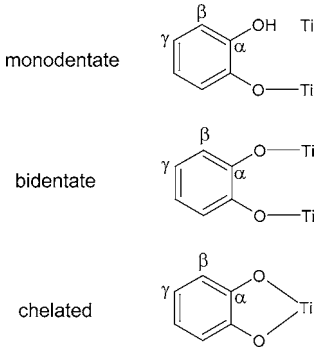

Figure 2. Possible binding modes of catechol on TiO_2.

adsorption have argued both in favor of a chelated structure[18−20] as well as in favor of a bidentate structure.[21−24] Scanning tunneling microscopy studies on atomically flat surfaces showed that catechol adopted a bidentate geometry with relatively high mobility on perfect surfaces, which became chelated and fixed when the molecule encountered a step.[25,26] This points to the defect concentration of the surface as a critical property for the bonding geometry. Monitoring of the Ti anchoring sites was also performed using XANES. Rajh et al. tracked the fate of the undercoordinated Ti^{3+} sites in aqueous nanoparticles and found that they disappeared upon adsorption of catechol, supporting a chelated geometry which restored the octahedral coordination present in the bulk.[9] Theoretical studies have addressed the optical activity of catechol−titania clusters[27] and shown that the local geometry of the substrate plays a key role in stabilizing chelated modes.[28]

Solid-state NMR spectroscopy is a powerful tool for obtaining molecular level details about ligands adsorbed on oxide surfaces.[29] However, it has not been used to elucidate the binding details of catechol on TiO_2, with very few studies applied to this or similar systems.[30−32] This is likely due to the fact that accurate and comprehensive simulations have to be performed in parallel to interpret the chemical shift distributions. The combination of experimental and theoretical NMR characterization has proven to reveal the local environment in a variety of chemical systems[33] and is the approach that will be followed in the present work to determine the binding mode of catechol on titania.

METHODS

Chemicals. Catechol was purchased from Alfa Aesar, and titanium tetrachloride from Sigma-Aldrich, and used as received. Catechol-d_2 was prepared by exchanging the hydroxyl protons in a D_2O solution (Alfa Aesar), obtaining a 97% degree of deuteration.

Synthesis of Nanoparticles. Ten milliliters of $TiCl_4$ was added dropwise to 200 mL of cold deionized water via a peristaltic pump. The $TiCl_4$ was cooled by a coldfinger, and the water was placed in an ice bath. The entire system was kept under N_2. Once all the $TiCl_4$ was added, the mixture was stirred for 10 min and placed in a dialysis bag. The water bath for dialysis was replaced until the pH of the nanoparticles was raised to 3.5.[9]

Capping of Nanoparticles. To prepare the capped nanoparticles, excess ligand was added to a solution of TiO_2, adjusted to pH 6, washed multiple times with water to remove excess ligand, and brought back to pH 3.5. The resulting material was dried one last time, crushed to a fine powder, and packed in a 4 mm NMR rotor.

UV−Vis. UV−vis spectra were measured with a PerkinElmer LAMBDA 1050 spectrometer in transmission mode with a 1 cm cuvette. As-synthesized nanoparticles are colloidal with a TiO_2 concentration of 0.2 M.

NMR. Solid-state NMR spectra were collected on a Varian 400 MHz wide bore spectrometer equipped with a 4 mm triple resonance probe configured for $^1H-^{13}C$ operation. ^{13}C CP MAS spectra were acquired at 10 kHz with a 2 ms contact time and two-pulse phase-modulated (TPPM) proton decoupling of 83 kHz during acquisition.[34] The recycle delays were 600 s for catechol crystal and 1 s for the capped TiO_2, reflecting the very different T_1 values. $\pi/2$ pulse lengths for ^1H and ^{13}C where 4.0 and 3.0 μs, respectively, and CP conditions were optimized by setting the ^{13}C power to 62.5 kHz and optimizing the ^1H power at the +1 sideband (72.5 kHz).

CP build-up curves were obtained in the 0 to 8 ms contact time range and fit with the IS* model because no characterstic oscillations could be observed either for the pure catechol or for the capped nanoparticles.

$$I(t_{CP}) = \frac{I_0}{1 - T_{IS}/T_{1\rho}}(e^{-t_{CP}/T_{1\rho}} - e^{-t_{CP}/T_{IS}}) \quad (1)$$

where I_0 is a scaling factor, T_{IS}^{-1} is the build-up rate, and $T_{1\rho}^{-1}$ is the spin−lattice relaxation rate in the rotating frame. The IS* model was fit to the data using a Marquardt−Levenberg procedure.[35]

To obtain the CSA parameters, slow-spinning spectra were acquired at 1.5, 1.9, and 2.5 kHz. CSA were then fit and simulated with TopSpin and DMfit.

DOI: 10.1021/acs.jpcc.6b08041
J. Phys. Chem. C 2016, 120, 23625−23630

COMPUTATIONAL METHODS AND MODELS

Energy. Calculations of the surface structures were carried out using the VASP 5.3.3 code[36,37] with the Perdew–Becke–Ernzerhof functional.[38] The core electrons were kept frozen by the plane-augmented wave method PAW.[39,40] The valence electrons (Ti $4s^2$ $3d^2$; O $2s^2$ $2p^4$; C $2s^2$ $2p^2$; H $1s^1$) are described explicitly by means of a plane-wave basis set with a cutoff of 400 eV. The reciprocal space was sampled with an adapted Monkhorst–Pack grid, with a distance of about 0.05 $Å^1$ between two *k*-points in the reciprocal space. Geometrical optimization was carried out using the conjugate-gradient algorithm with a tolerance of 0.1 meV in total energy. Dipole corrections were included in the direction perpendicular to the slab. All the atoms of the system were allowed to relax. A four-TiO_2 layer thick model was used to compute the adsorption geometries and energies. From the optimized structures, the slabs were cut to generate two-TiO_2 layer thick models that were again optimized and then used for the NMR calculations.

NMR Shifts. The Quantum Espresso package[41] was used to perform the NMR calculations, with the PBE functional.[38] A plane wave basis set of cutoff 816 eV was used together with pseudopotentials to represent the core electrons.[42,43] The gauge including projector augmented wave (GIPAW) method[44] was employed to obtain the shielding tensor. These calculations were performed on the small models (two-TiO_2 layers thick) previously optimized with VASP, due to the high computational demand of this type of calculation. The ^{13}C chemical shifts are related to the shielding tensor by a linear relation that was obtained using catechol crystal as a standard. This was chosen because we are only interested in the chemical shift differences from the catechol in the gas phase and not comparison between different models. A comparison with linear relations obtained with a library of molecules, however, yielded negligible differences. The linear relation used was $\delta = -0.8873\sigma + 163.24$ where δ and σ are the ^{13}C chemical shift and shielding tensor, respectively.

Models. Three terminations of the anatase TiO_2 were considered for the periodic slab models: (001), (100), and (101). Four-TiO_2 layer thick models were used, obtained from ref 21. In a first step they were fully optimized and the adsorption energy of catechol was calculated as the difference in energy between the catechol slab and the sum of bare slab plus gas-phase catechol (negative values indicate favorable interaction). Molecular, bidentate, monodentate, and chelated geometries were explored on regular stoichiometric bulk-cut slabs. The catechol molecule was fully deprotonated in the bidentate and chelated mode, deprotonated once in the monodentate mode, and neutral in the molecular mode. Upon deprotonation, the H^+ binds to surface undercoordinated oxygen sites, and the catecholate forms O–Ti bonds, as found for similar systems in periodic[21,45,46] and cluster models.[27,28,47] To take into account defective surfaces, three models were constructed for the (101), (001), and (100) terminations, in which a TiO_2 unit was removed from the top layer. During the optimization, only the (001)-terminated slab stabilized the chelated mode; the others evolved to bidentate species. The coordinates of the model for the stepped (001) slab with a chelated species is included in Supporting Information (SI). In a second step the optimized structures were used to construct smaller models compatible with the high computational cost of the GIPAW calculation; the lower half of the slab was cut, and the new system geometry was optimized. Consistency was checked between the two sets of models in regard to geometry, adsorption energy, and NMR predictions while large differences existed in the forces present and the energies, and the NMR predictions agreed within 1%. This computational protocol has been successfully applied recently to characterize phosphate species on TiO_2.[32]

RESULTS AND DISCUSSION

Anatase nanoparticles 4.6 ± 1 nm in diameter were synthesized and functionalized with catechol as detailed in Methods (see Figure 3). The anatase bandgap is strongly red-shifted upon

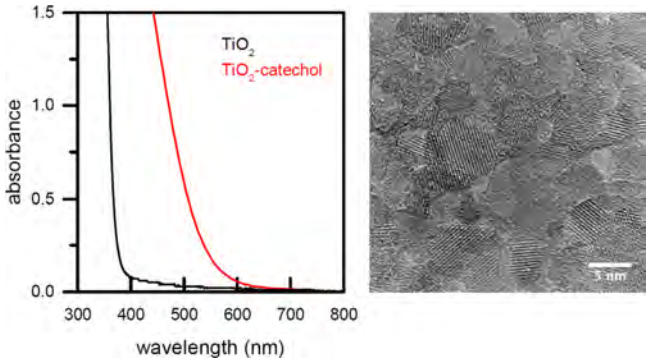

Figure 3. Left: UV–vis of TiO_2 without (black) and with (red) catechol. Right: TEM of TiO_2 nanoparticles. Size analysis yields nanoparticles with a diameter of 4.6 ± 1 nm.

catechol addition (see Figure 3). The LUMO of the catechol is strongly coupled to the conduction band via the oxygens, resulting in a newly formed charge-transfer state that has an absorption in the visible.[9] To assign a geometry to the catechol–TiO_2 complex, we turn to NMR spectroscopy.

Solid-State NMR. The ^{13}C CP-MAS spectrum of catechol and catechol on TiO_2 is shown in Figure 4. For pure catechol, we see three sharp peaks for the three distinct carbons in

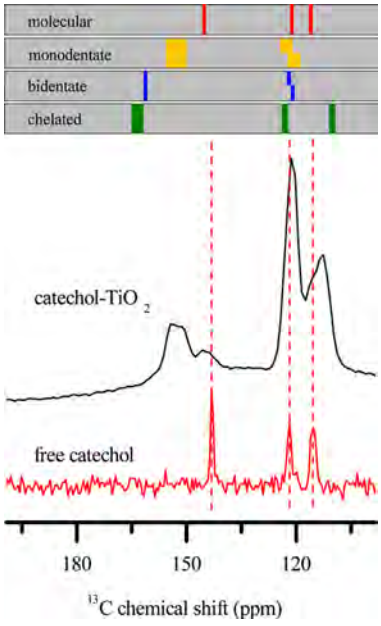

Figure 4. Ten kilohertz ^{13}C CP-MAS spectra of catechol and TiO_2–catechol. Traces are offset vertically for clarity. The top shows chemical shift predictions from ab initio calculations.

DOI: 10.1021/acs.jpcc.6b08041
J. Phys. Chem. C 2016, 120, 23625–23630

catechol. Upon adsorption, the α- and β-carbons are split into two peaks corresponding to two different speciations, that we call species I and species II (see Table 1). The α-carbon has

Table 1. Measured Chemical Shifts for Native Catechol and Catechol on TiO_2

	α-carbon	β-carbon	γ-carbon
native catechol	143	116	121
catechol–TiO_2 I	154	110	121
catechol–TiO_2 II	145	116	121

two downfield shifts from 143 to 145 ppm and 154 ppm, while the β-carbon has chemical shifts at 116 ppm (unchanged from native catechol) and an upfield shift at 110 ppm. The γ-carbon at 121 ppm does not shift in position. To assist in the assignment of the adsorbed species, we carry out an exhaustive computational exploration of catechol binding on TiO_2 facets.

DFT and Chemical Shift Prediction. The molecular, monodentate, bidentate, and chelated adsorption modes were computed on the different slab models (Figure 5). The full

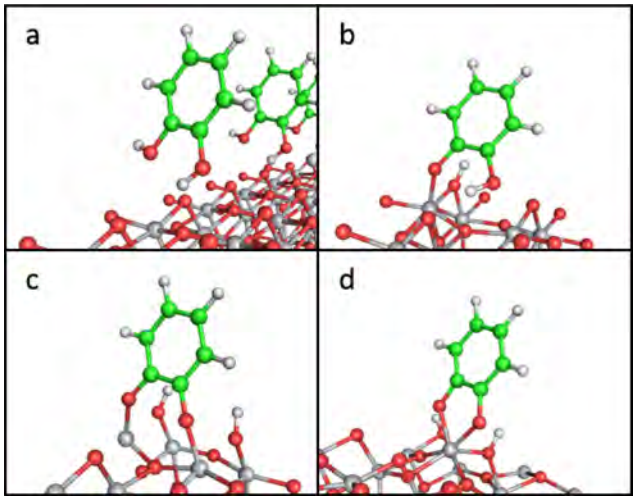

Figure 5. Adsorption geometries on the {101} facet for (a) molecular, (b) monodentate, (c) bidentate, and (d) chelated modes.

chemical shift tensors are reported in Table 2 together with the adsorption energies found for the large and small slab models. As can be seen, the adsorption energy found for both large and small slabs are in good agreement. The values for adsorption energy become more exothermic (negative) for the series (101) < (100) < (001) and were also found for the adsorption of neutral dopamine.[21] The general trend is the stabilization of bidentate modes, with adsorption energies in the range [−1.84:−0.65] eV, followed by monodentate in the range [−0.90:−0.62] eV, molecular [−0.33:−0.14] eV and chelated ones [−0.62:0.24] eV. It is interesting to note that the chelated modes are the least stable ones, although they compete with the monodentate ones in the termination (001). The chelated geometry on a defective (001) model shows a very exothermic adsorption energy reaching −1.58 eV. We conclude that the presence of surface defective sites, involving low coordination for titanium sites, stabilizes the chelated structures. A recent work using small titania clusters[28] shows that the chelated geometry may become the preferred adsorption mode depending on the local surface structure, with direct implication in the absorption spectra. In titania nanoparticles like those studied here, the presence of undercoordinated surface titania sites is likely to occur, whereas regular terminations are expected to be less common.

An analysis of the results in Table 2 shows the following trends. First, the α-carbon is always displaced downfield upon adsorption for chelated, bidentate, or monodentate. The β-carbon is shifted slightly downfield for the molecular, monodentate, or bidentate case but is shifted upfield for the chelated geometry. Finally, the γ-carbon is perturbed negligibly by the interaction with the surface. Comparison between experiment and theory shows that only the chelated structure can account for the chemical shifts of species I. Species II has its α-carbon shifted slightly downfield, while the other carbons remain at the same positions as in native catechol. Monodentate or molecular catechol is consistent with these changes.

Contact Times. The magnetization transfer from ^1H to ^{13}C spins occurs via through-space dipole–dipole interactions and follows a $1/r^6$ dependence on the interspin distance r. The build-up kinetics, where the ^{13}C magnetization is monitored as a function of the duration of the magnetization transfer window, can be used to determine the presence of nearby ^1H spins.[35] In our case we can use these experiments to determine the protonation state of the nearby oxygens. Build-up curves were measured for catechol, catechol-d_2, and catechol–TiO_2 (see Figure 6A,B) and fitted to the IS* model (see Table 3). We focus on the α-carbons only due to their proximity to the oxygen sites. The possibility of comparing H_2-catechol and catechol-d_2 allows us to estimate the contribution of the hydroxyl hydrogens to the build-up rates. These can be decomposed into the contributions from the OH groups ($1/T_{(OH)_2}$), and the rest of the molecule or molecule/surface ($1/T_{\text{catechol-}d_2}$):

$$1/T_{\text{catechol}} = 1/T_{\text{catechol-}d_2} + 1/T_{(OH)_2} \quad (2)$$

For the catechol crystal, the contribution of the hydroxyl groups is 1.06 ms^{-1}. Once adsorbed, the long relaxation times for neat catechol arising from the rigidity of the crystal become finite and <10s. Also, upon adsorption to the surface, the build-up rates increase. Given our initial preparation conditions (pH = 3.5), we attribute this general increase to the presence of surface OH groups and adsorbed water molecules.[48] We can also calculate the difference in rates between the two α-carbon signals of adsorbed species (species I and II) and find it to be 1.28 ms^{-1}, with the most downfield signal having the longer build-up time constant. The similarity of this rate to the contribution of the hydroxyl protons tells us that species I has two less protons on the oxygens than species II, so that species I is doubly deprotonated consistent with a chelated geometry as observed from the chemical shifts, or a bidentate geometry; species II is a fully protonated (or molecular) species. This is a similar conclusion reached by Lana-Villareal et al.[20] using IR and Raman spectroscopies and in contrast with other studies.[21−24] It is possible that during the drying process bidentate or monodentate species become protonated, appearing in our measurement as molecular species.

Chemical Shift Anisotropies. Chemical shift anisotropies are also very reliable signatures of the binding modes and are reported for completion in Table 2 using the Herzfeld–Berger convention. The distinctive signature of a chelated geometry is a negative asymmetry parameter κ of the α-carbon and an

DOI: 10.1021/acs.jpcc.6b08041
J. Phys. Chem. C 2016, 120, 23625−23630

Table 2. Adsorption Energy E_{ads} in eV for the Large and Small Model (see text), and Full Chemical Shift Tensor Parameters Obtained from DFT calculations for the Small Models[a]

		E_{ads}		α-carbon			β-carbon			γ-carbon		
facet	binding mode	large	small	δ_{iso}	Ω	κ	δ_{iso}	Ω	κ	δ_{iso}	Ω	κ
(101)	bidentate	−0.66	−0.45	161	127	0.62	121	155	0.26	123	198	0.13
(100)	bidentate	−1.15	−1.06	162	128	0.64	121	155	0.29	122	196	0.14
(001)	bidentate	−1.84	−1.57	161	125	0.63	120	156	0.27	122	196	0.13
(101)	chelated	0.24	0.23	162	135	−0.21	110	138	0.38	123	204	0.04
(100)	chelated	−0.01	−0.06	165	134	0.07	110	140	0.36	123	201	0.06
(001)	chelated	−0.84	−0.79	162	142	−0.33	110	140	0.40	123	204	0.05
(101)-defect	chelated	to bidentate	-	-	-	-	-	-	-	-	-	-
(001)-defect	chelated	−1.58	−1.57	162	130	−0.01	110	143	0.30	124	202	0.11
(100)-defect	chelated	to bidentate	-	-	-	-	-	-	-	-	-	-
(101)	monodentate	−0.37	−0.62	155	129	0.33	122	163	0.27	124	200	0.14
(100)	monodentate	to bidentate	-	-	-	-	-	-	-	-	-	
(001)	monodentate	−0.85	−0.90	150	125	0.42	119	155	0.11	121	196	0.13
(101)	molecular	−0.32	−0.29	145	131	0.30	116	159	0.18	121	196	0.13
(100)	molecular	−0.14	−0.33	146	135	0.36	115	159	0.19	120	196	0.10
(001)	molecular	−0.25	−0.24	146	137	0.32	116	163	0.21	121	198	0.12

[a]The reported values are the average values over the pairs of identical spins of catechol. For the full value of chemical shifts, see SI.

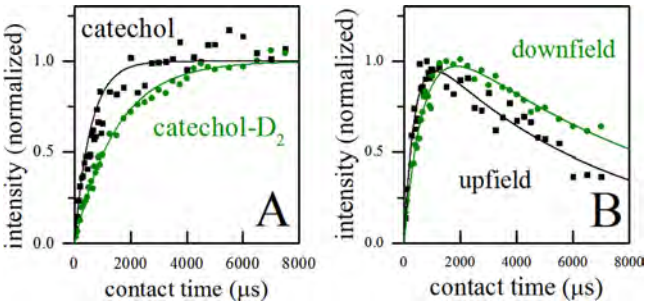

Figure 6. Contact times build-up for the α-carbons catechol and catechol-d_2 (left) and of the two conformers on TiO_2 (right).

Table 3. Parameters of the IS* Model

	T_{IS} (μs)	$T_{1\rho}$ (μs)
catechol	581 ± 16	∞
catechol-d_2	1501 ± 21	∞
catechol−TiO_2, upfield	370 ± 38	6484 ± 636
catechol−TiO_2, downfield	679 ± 48	8546 ± 906

upfield chemical shift of the β-carbon. CSA experiments were not found to be conclusive due to peak crowding (see Supporting Information); nonetheless, the theoretical values are reported for completion should they prove useful for subsequent work.

Defective Surfaces. Since catechol binds in a chelated geometry preferentially on defective surfaces, we constructed models of defects on the three structures of TiO_2 (results reported in Table 2 for compactness). The models constructed for (101) and (100) terminations evolved during the optimization to bidentate modes. We notice that the upfield shift of the γ-carbon characteristic of a chelated geometry is present on the {001} facet. Furthermore, the strongly negative value of the skew parameter κ from pristine surfaces becomes almost null for (001) in agreement with the CSA pattern estimations and slightly positive for the (100) (see SI). Such an agreement with the (001) surface would seem to suggest that defects are more common on the (001) surface, where it is known that 4-fold coordinated Ti appears in typical reconstructions.[49] These results show that not only the adsorption mode but also the local substrate structure has a strong impact on the chemical shifts and in particular the anisotropy of the magnetic tensor. This is not obvious from the result of defect-free slabs where the chemical shifts are not strongly surface dependent (see Table 2).

CONCLUSION

We have applied solid-state NMR techniques coupled to DFT-GIPAW chemical shift predictions to the binding of catechol on TiO_2. On the basis of ^{13}C chemical shifts, we conclude that chelated species are unambiguously present on the surface. By analyzing the build-up curves, we can assign the protonation state of the second species as doubly protonated at the oxygen positions and assign it to a molecular species. More in-depth models of the facets with defects suggest that the chelated species are most likely adsorbed on defective (001) sites. Finally, because of peak overlaps it is possible that some degree of bidentate structures are also present. The combination of a chelated and molecular species is the simplest model that explains our observations. These apply to dried samples and it is possible that other geometries exist in a dynamic equilibrium in solution. This is one of the few reports providing direct experimental evidence of the presence of chelated geometries. Our work is a stepping stone for the analysis of further ligands, not only to help understand the details of the adsorption geometry but also of the dynamics which might be crucial in photocatalytic systems where adsorption of reactants is often the rate-limiting step.

ASSOCIATED CONTENT

Supporting Information

The Supporting Information is available free of charge on the ACS Publications website at DOI: 10.1021/acs.jpcc.6b08041.

Selective dynamics (TXT)

Chemical shift anisotropy experiments and a full table of calculated chemical shifts (PDF)

DOI: 10.1021/acs.jpcc.6b08041
J. Phys. Chem. C 2016, 120, 23625−23630

AUTHOR INFORMATION

Corresponding Author

*E-mail: dfs@asu.edu. Phone: +0046 721-889855.

Present Addresses

[#]Daniel Finkelstein-Shapiro, Division of Chemical Physics, Lund University, Box 124, 221 00 Lund, Sweden.

[∇]Stephen K. Davidowski, Department of Chemistry, University of Washington, Seattle, Washington 98195, United States.

Notes

The authors declare no competing financial interest.

ACKNOWLEDGMENTS

We thank Christel Gervais for stimulating discussions on the GIPAW method. This work was performed using HPC resources from GENCI- CINES/IDRIS (Grant 2015-x2015082131, 2014- x2014082131) and the CCRE-DSI of Université P. M. Curie. M.C. is grateful to Dr. B. Diawara for the Modelview program used in the construction of the models. D.F.S. acknowledges the program "Research in Paris" for a fellowship.

REFERENCES

(1) Gratzel, M. *J. Photochem. Photobiol., C* **2003**, *4*, 145−153.
(2) Duncan, W. R.; Prezhdo, O. V. *J. Phys. Chem. B* **2005**, *109*, 365−373.
(3) Galoppini, E. *Coord. Chem. Rev.* **2004**, *248*, 1283−1297.
(4) Megiatto, J. D., Jr.; Méndez-Hernández, D. D.; Tejeda-Ferrari, M. E.; Teillout, A.-L.; Llansola-Portolés, M. J.; Kodis, G.; Poluektov, O. G.; Rajh, T.; Mujica, V.; Groy, T. L.; Gust, D.; Moore, T. A.; Moore, A. L. *Nat. Chem.* **2014**, *6*, 423−428.
(5) Graetzel, M. *J. Photochem. Photobiol., A* **2004**, *164*, 3−14.
(6) Tachan, Z.; Hod, I.; Zaban, A. *Adv. Energy Mater.* **2014**, *4*, 1301249.
(7) Finkelstein-Shapiro, D.; Petrosko, S. H.; Dimitrijevic, N. M.; Gosztola, D.; Gray, K. A.; Rajh, T.; Tarakeshwar, P.; Mujica, V. *J. Phys. Chem. Lett.* **2013**, *4*, 475−479.
(8) Rangan, S.; Theisen, J.-P.; Bersch, E.; Bartynski, R. *Appl. Surf. Sci.* **2010**, *256*, 4829−4833.
(9) Rajh, T.; Chen, L. X.; Lukas, K.; Liu, T.; Thurnauer, M. C.; Tiede, D. M. *J. Phys. Chem. B* **2002**, *106*, 10543−10552.
(10) Musumeci, A.; Gosztola, D.; Schiller, T.; Dimitrijevic, N. M.; Mujica, V.; Martin, D.; Rajh, T. *J. Am. Chem. Soc.* **2009**, *131*, 6040−6041.
(11) Tarakeshwar, P.; Palma, J. L.; Finkelstein-Shapiro, D.; Keller, A.; Urdaneta, I.; Calatayud, M.; Atabek, O.; Mujica, V. *J. Phys. Chem. C* **2014**, *118*, 3774−3782.
(12) Fano, U. *Phys. Rev.* **1961**, *124*, 1866.
(13) Finkelstein-Shapiro, D.; Urdaneta, I.; Calatayud, M.; Atabek, O.; Mujica, V.; Keller, A. *Phys. Rev. Lett.* **2015**, *115*, 113006.
(14) Sánchez-de-Armas, R.; Oviedo Lopez, J.; A San-Miguel, M.; Sanz, J. F.; Ordejon, P.; Pruneda, M. *J. Chem. Theory Comput.* **2010**, *6*, 2856−2865.
(15) An, B.-K.; Hu, W.; Burn, P. L.; Meredith, P. *J. Phys. Chem. C* **2010**, *114*, 17964−17974.
(16) Nazeeruddin, M. K.; De Angelis, F.; Fantacci, S.; Selloni, A.; Viscardi, G.; Liska, P.; Ito, S.; Takeru, B.; Graetzel, M. *J. Am. Chem. Soc.* **2005**, *127*, 16835−16847.
(17) Moser, J.; Punchihewa, S.; Infelta, P. P.; Graetzel, M. *Langmuir* **1991**, *7*, 3012−3018.
(18) Redfern, P. C.; Zapol, P.; Curtiss, L. A.; Rajh, T.; Thurnauer, M. C. *J. Phys. Chem. B* **2003**, *107*, 11419−11427.
(19) Tarakeshwar, P.; Finkelstein-Shapiro, D.; Rajh, T.; Mujica, V. *Int. J. Quantum Chem.* **2011**, *111*, 1659−1670.
(20) Lana-Villarreal, T.; Rodes, A.; Pérez, J. M.; Gómez, R. *J. Am. Chem. Soc.* **2005**, *127*, 12601−12611.
(21) Urdaneta, I.; Keller, A.; Atabek, O.; Palma, J. L.; Finkelstein-Shapiro, D.; Tarakeshwar, P.; Mujica, V.; Calatayud, M. *J. Phys. Chem. C* **2014**, *118*, 20688−20693.
(22) Rodriguez, R.; Blesa, M. A.; Regazzoni, A. E. *J. Colloid Interface Sci.* **1996**, *177*, 122−131.
(23) Savic, T. D.; Jankovic, I. A.; Saponjic, Z. V.; Comor, M. I.; Veljkovic, D. Z.; Zaric, S. D.; Nedeljkovic, J. M. *Nanoscale* **2012**, *4*, 1612−1619.
(24) Savic, T. D.; Comor, M. I.; Nedeljkovic, J. M.; Veljkovic, D. Z.; Zaric, S. D.; Rakic, V. M.; Jankovic, I. A. *Phys. Chem. Chem. Phys.* **2014**, *16*, 20796−20805.
(25) Li, S.-C.; Wang, J.-g.; Jacobson, P.; Gong, X.-Q.; Selloni, A.; Diebold, U. *J. Am. Chem. Soc.* **2009**, *131*, 980−984.
(26) Liu, L.-M.; Li, S.-C.; Cheng, H.; Diebold, U.; Selloni, A. *J. Am. Chem. Soc.* **2011**, *133*, 7816−7823.
(27) Sanchez-de Armas, R.; San-Miguel, M. A.; Oviedo, J.; Marquez, A.; Sanz, J. F. *Phys. Chem. Chem. Phys.* **2011**, *13*, 1506−1514.
(28) Luppi, E.; Urdaneta, I.; Calatayud, M. *J. Phys. Chem. A* **2016**, *120*, 5115−5124.
(29) Holland, G. P.; Sharma, R.; Agola, J. O.; Amin, S.; Solomon, V. C.; Singh, P.; Buttry, D. A.; Yarger, J. L. *Chem. Mater.* **2007**, *19*, 2519−2526.
(30) Tachikawa, T.; Takai, Y.; Tojo, S.; Fujitsuka, M.; Majima, T. *Langmuir* **2006**, *22*, 893−896.
(31) Park, T.-J.; Kim, J.; Kim, T.-K.; Park, H.-M.; Choi, S.-S.; Kim, Y. *Bull. Korean Chem. Soc.* **2008**, *29*, 2459.
(32) Tielens, F.; Gervais, C.; Deroy, G.; Jaber, M.; Stievano, L.; Coelho Diogo, C.; Lambert, J.-F. *Langmuir* **2016**, *32*, 997−1008.
(33) Bonhomme, C.; Gervais, C.; Babonneau, F.; Coelho, C.; Pourpoint, F.; Azais, T.; Ashbrook, S. E.; Griffin, J. M.; Yates, J. R.; Mauri, F.; Pickard, C. J. *Chem. Rev.* **2012**, *112*, 5733−5779.
(34) Bennett, A. E.; Rienstra, C. M.; Auger, M.; Lakshmi, K. V.; Griffin, R. G. *J. Chem. Phys.* **1995**, *103*, 6951−6958.
(35) Kolodziejski, W.; Klinowski, J. *Chem. Rev.* **2002**, *102*, 613−628.
(36) Kresse, G.; Furthmüller, J. *Phys. Rev. B: Condens. Matter Mater. Phys.* **1996**, *54*, 11169−11186.
(37) Kresse, G.; Hafner, J. *Phys. Rev. B: Condens. Matter Mater. Phys.* **1993**, *48*, 13115−13118.
(38) Perdew, J. P.; Burke, K.; Ernzerhof, M. *Phys. Rev. Lett.* **1996**, *77*, 3865−3868.
(39) Blöchl, P. E. *Phys. Rev. B: Condens. Matter Mater. Phys.* **1994**, *50*, 17953−17979.
(40) Kresse, G.; Joubert, D. *Phys. Rev. B: Condens. Matter Mater. Phys.* **1999**, *59*, 1758−1775.
(41) Giannozzi, P.; et al. *J. Phys.: Condens. Matter* **2009**, *21*, 395502.
(42) Troullier, N.; Martins, J. L. *Phys. Rev. B: Condens. Matter Mater. Phys.* **1991**, *43*, 1993−2006.
(43) Kleinman, L.; Bylander, D. M. *Phys. Rev. Lett.* **1982**, *48*, 1425−1428.
(44) Pickard, C. J.; Mauri, F. *Phys. Rev. B: Condens. Matter Mater. Phys.* **2001**, *63*, 245101.
(45) Di Valentin, C.; Fittipaldi, D. *J. Phys. Chem. Lett.* **2013**, *4*, 1901−1906.
(46) Calatayud, M.; Minot, C. *Top. Catal.* **2006**, *41*, 17−26.
(47) Sanchez-de Armas, R.; San-Miguel, M. A.; Oviedo, J.; Marquez, A.; Sanz, J. F. *Phys. Chem. Chem. Phys.* **2011**, *13*, 1506−1514.
(48) Nosaka, A. Y.; Fujiwara, T.; Yagi, H.; Akutsu, H.; Nosaka, Y. *J. Phys. Chem. B* **2004**, *108*, 9121−9125.
(49) Wang, Y.; Sun, H.; Tan, S.; Feng, H.; Cheng, Z.; Zhao, J.; Zhao, A.; Wang, B.; Luo, Y.; Yang, J.; Hou, J. G. *Nat. Commun.* **2013**, *4*, 1−8.

DOI: 10.1021/acs.jpcc.6b08041
J. Phys. Chem. C 2016, 120, 23625−23630